

Breathing Mode Dynamics and Elastic Properties of Gold Nanoparticles

Charles F. Vardeman II, Patrick F. Conforti, Megan M. Sprague, and J. Daniel Gezelter*

Department of Chemistry and Biochemistry, University of Notre Dame, Notre Dame, Indiana 46556

Received: March 28, 2005

We present calculations of the bulk modulus, heat capacity, and the period of the breathing mode for spherical nanoparticles following excitation by ultrafast laser pulses. The bulk modulus and heat capacities both exhibit clear transitions upon bulk melting of the particles. Equilibrium calculations of the heat capacity show that the melting transition is sharper and occurs at a lower temperature than one would observe from an ultrafast experiment. We also observe an intriguing splitting in the low-frequency spectra of the nanoparticles and analyze this splitting in terms of Lamb's classical theory of elastic spheres. We conclude that the particles either (1) melt during the observation period following laser excitation or (2) melt an outer shell while maintaining a crystalline core. Both mechanisms for melting are commensurate with our observations.

1. Introduction

In metallic nanoparticles, the relatively large surface area-to-volume ratio induces a number of well-known size-dependent phenomena. Notable among these are the depression of the bulk melting temperature,^{1–3} surface melting transitions, increased room-temperature alloying rates,⁴ changes in the breathing mode frequencies,^{5–8} and rapid heat transfer to the surrounding medium.^{9,10}

This paper reports on atomic-level simulations of the transient response of metallic nanoparticles to the nearly instantaneous heating undergone when photons are absorbed during ultrafast laser excitation experiments. The time scale for heating (determined by the *e-ph* coupling constant) is faster than a single period of the breathing mode for spherical nanoparticles.^{11,12} Hot-electron pressure and direct lattice heating contribute to the thermal excitation of the atomic degrees of freedom, and both mechanisms are rapid enough to coherently excite the breathing mode of the spherical particles.¹³

There are questions posed by the experiments that may be easiest to answer via computer simulation. For example, the dephasing seen following coherent excitation of the breathing mode may be due to inhomogeneous size distributions in the sample, but it may also be due to softening of the breathing mode vibrational frequency following a melting transition. Additionally, there are properties (such as the bulk modulus) that may be nearly impossible to obtain experimentally, but which are relatively easily obtained via simulation techniques.

We outline our simulation techniques in section 2. Results are presented in section 3. We discuss our results in terms of Lamb's classical theory of elastic spheres in section 4.

2. Computational Details

Spherical Au nanoparticles were created in a standard FCC lattice at four different radii [20 Å (1926 atoms), 25 Å (3884 atoms), 30 Å (6602 atoms), and 35 Å (10606 atoms)]. To create spherical nanoparticles, a large FCC lattice was built at the normal Au lattice spacing (4.08 Å) and any atoms outside the target radius were excluded from the simulation.

2.1. Simulation Methodology. Potentials were calculated using the Voter–Chen parametrization¹⁴ of the Embedded Atom

Method (EAM), which has been widely used for MD simulations of metallic particles.^{14–18} Like other transition metal potentials,^{19–23} EAM describes bonding in metallic systems by including an attractive interaction that models the stabilization of a positively charged metal core ion in a sea of surrounding valence electrons. A repulsive pair potential describes the interactions of the core ions with each other. The EAM potential has the form:

$$V = \sum_i F_i[\rho_i] + \sum_i \sum_{j \neq i} \phi_{ij}(\mathbf{r}_{ij}) \quad (1)$$

$$\rho_i = \sum_{j \neq i} f_j(\mathbf{r}_{ij}) \quad (2)$$

where ϕ_{ij} is the (primarily repulsive) pairwise interaction between atoms *i* and *j*. $F_i[\rho_i]$ is an embedding function that determines the energy to embed the positively charged core, *i*, in the electron density, ρ_i , due to the valence electrons of the surrounding *j* atoms, and $f_j(r)$ describes the radial dependence of the field due to atom *j*. There is a cutoff distance, r_{cut} , that limits the summations in the EAM equation to the few dozen atoms surrounding atom *i*. In these simulations, a cutoff radius of 5.55 Å was used.

Before starting the molecular dynamics runs, a relatively short steepest-descent minimization was performed to relax the lattice in the initial configuration. To facilitate the study of the larger particles, simulations were run in parallel over 16 processors, using Plimpton's force-decomposition method.²⁴

To mimic the events following the absorption of light in the ultrafast laser heating experiments, we have used a simple two-step process to prepare the simulations. Instantaneous heating of the lattice was performed by sampling atomic velocities from a Maxwell–Boltzmann distribution set to twice the target temperature for the simulation. By equipartition, approximately half of the initial kinetic energy of the system winds up in the potential energy of the system. The system was allowed a very short (10 fs) evolution period with the new velocities.

Following this excitation step, the particles evolved under Nosé–Hoover NVT dynamics²⁵ for 40 ps. Given the mass of the constituent metal atoms, time steps of 5 fs give excellent energy conservation in standard NVE integrators, so the same

time step was used in the NVT simulations. Target temperatures for these particles spanned the range from 300 to 1350 K in 50 K intervals. Five independent samples were run for each particle and temperature. The results presented below are averaged properties for each of the five independent samples.

2.2. Analysis. Of primary interest when comparing our simulations to experiments is the dynamics of the low-frequency breathing mode of the particles. To study this motion, we need access to accurate measures of both the volume and surface area as a function of time. Throughout the simulations, we monitored both quantities using Barber et al.'s very fast quickhull algorithm to obtain the convex hull for the collection of 3-d coordinates of all of the atoms at each point in time.^{26,27} The convex hull is the smallest convex polyhedron that includes all of the atoms, so the volume of this polyhedron is an excellent estimate of the volume of the nanoparticle. The convex hull estimate of the volume will be problematic if the nanoparticle breaks into pieces (i.e., if the bounding surface becomes concave), but for the relatively short trajectories of this study, it provides an excellent measure of particle volume as a function of time.

The bulk modulus, which is the inverse of the compressibility,

$$K = \frac{1}{\kappa} = -V \left(\frac{\partial P}{\partial V} \right)_T \quad (4)$$

can be related to quantities that are relatively easily accessible from our molecular dynamics simulations. We present here four different approaches for estimating the bulk modulus directly from basic or derived quantities:

(1) The traditional “energetic” approach: Using basic thermodynamics and one of the Maxwell relations, we write

$$P = T \left(\frac{\partial S}{\partial V} \right)_T - \left(\frac{\partial U}{\partial V} \right)_T \quad (4)$$

It follows that

$$K = V \left(T \left(\frac{\partial^2 S}{\partial V^2} \right)_T + \left(\frac{\partial^2 U}{\partial V^2} \right)_T \right) \quad (5)$$

The standard practice in solid-state physics is to assume the low-temperature limit (i.e., to neglect the entropic term), which means the bulk modulus is usually expressed as

$$K \approx V \left(\frac{\partial^2 U}{\partial V^2} \right)_T \quad (6)$$

When the relationship between the total energy U and volume V of the system is available at a fixed temperature (as it is in these simulations), it is a simple matter to compute the bulk modulus from the response of the system to the perturbation of the instantaneous heating. Although this information would, in theory, be available from longer constant temperature simulations, the ranges of volumes and energies explored by a nanoparticle under equilibrium conditions are actually quite small. Instantaneous heating, since it excites coherent oscillations in the breathing mode, allows us to sample a much wider range of volumes (and energies) for the particles. The problem with this method is that it neglects the entropic term near the melting transition, which gives spurious results (negative bulk moduli) at higher temperatures.

(2) The linear response approach: Linear response theory gives us another approach to calculating the bulk modulus. This

method relates the low-wavelength fluctuations in the density to the isothermal compressibility,²⁸

$$\lim_{k \rightarrow 0} \langle |\delta \rho(\vec{k})|^2 \rangle = \frac{k_B T \rho^2 \kappa}{V} \quad (7)$$

where the frequency dependent density fluctuations are the Fourier transform of the spatial fluctuations,

$$\delta \rho(\vec{k}) = \int_V e^{i\vec{k} \cdot \vec{r}} (\rho(\vec{r}, t) - \langle \rho \rangle) dV \quad (8)$$

This approach is essentially equivalent to using the volume fluctuations directly to estimate the bulk modulus,

$$K = \frac{V k_B T}{\langle \delta V^2 \rangle} = k_B T \frac{\langle V \rangle}{\langle V^2 \rangle - \langle V \rangle^2} \quad (9)$$

It should be noted that in these experiments, the particles are *far from equilibrium*, and so a linear response approach will not be the most suitable way to obtain estimates of the bulk modulus.

(3) The extended system approach: Since we are performing these simulations in the NVT ensemble using Nosé–Hoover thermostating, the quantity conserved by our integrator (H_{NVT}) can be expressed as:

$$H_{\text{NVT}} = U + f k_B T_{\text{ext}} \left(\frac{\tau_T^2 \chi(t)^2}{2} + \int_0^t \chi(s) ds \right) \quad (10)$$

Here f is the number of degrees of freedom in the (real) system, T_{ext} is the temperature of the thermostat, τ_T is the time constant for the thermostat, and $\chi(t)$ is the instantaneous value of the extended system thermostat variable. The extended Hamiltonian for the system, H_{NVT} , is, to within a constant, the Helmholtz free energy.²⁹ Since the pressure is a simple derivative of the Helmholtz free energy,

$$P = - \left(\frac{\partial A}{\partial V} \right)_T \quad (11)$$

the bulk modulus can be obtained (theoretically) by a quadratic fit of the fluctuations in H_{NVT} against fluctuations in the volume,

$$K = -V \left(\frac{\partial^2 H_{\text{NVT}}}{\partial V^2} \right)_T \quad (12)$$

However, H_{NVT} is essentially conserved during these simulations, so fitting fluctuations of this quantity to obtain meaningful physical quantities is somewhat suspect. We also note that this method would fail in periodic systems because the volume itself is fixed in periodic NVT simulations.

(4) The direct pressure approach: Our preferred method for estimating the bulk modulus is to compute it *directly* from the internal pressure in the nanoparticle. The pressure is obtained via the trace of the pressure tensor,

$$P = \frac{1}{3} \text{Tr}[\vec{\mathbf{P}}] \quad (13)$$

which has a kinetic contribution as well as a contribution from the stress tensor ($\vec{\mathbf{W}}$):

$$\vec{\mathbf{P}} = \frac{1}{V} \left(\sum_{i=1}^N m_i \vec{v}_i \otimes \vec{v}_i \right) + \vec{\mathbf{W}} \quad (14)$$

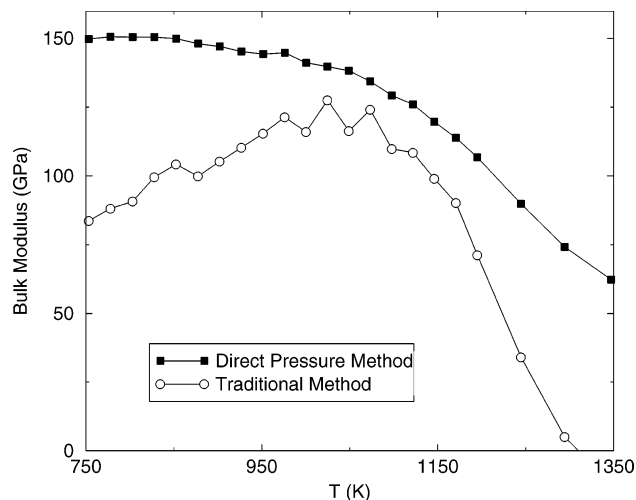


Figure 1. Comparison of two of the methods for estimating the bulk modulus as a function of temperature for the 35 Å particle.

Here the \otimes symbol represents the *outer* product of the velocity vector for atom i to yield a 3×3 matrix. The virial is computed during the simulation using forces between pairs of particles,

$$\vec{W} = \sum_i \sum_{j>i} \vec{r}_{ij} \otimes \vec{f}_{ij} \quad (15)$$

During the simulation, we record the internal pressure, P , as well as the total energy, U , the extended system's Hamiltonian, H_{NVT} , and the particle coordinates. Once we have calculated the time-dependent volume of the nanoparticle using the convex hull, we can use any of these four methods to estimate the bulk modulus.

We find, however, that only the fourth method (the direct pressure approach) gives meaningful results. Bulk moduli for the 35 Å particle were computed with the traditional (energy vs volume) approach as well as the direct pressure approach. A comparison of the bulk modulus obtained via both methods is shown in Figure 1. Note that the second derivative fits in the traditional approach can give (in the liquid droplet region) negative curvature, and this results in negative values for the bulk modulus. The Bulk moduli reported in the rest of this paper were computed using the direct pressure method.

To study the frequency of the breathing mode, we have calculated the power spectrum for volume (V) fluctuations,

$$\rho_{\Delta V}(\omega) = \int_{-\infty}^{\infty} \langle \Delta V(t) \Delta V(0) \rangle e^{-i\omega t} dt \quad (16)$$

where $\Delta V(t) = V(t) - \langle V \rangle$. Because the instantaneous heating excites all of the vibrational modes of the particle, the power spectrum will contain contributions from all modes that perturb the total volume of the particle. The lowest frequency peak in the power spectrum should give the frequency (and period) for the breathing mode, and these quantities are most readily compared with the Hartland group experiments.¹² Further analysis of the breathing dynamics follows in section 4.

We have also computed the heat capacity for our simulations to verify the location of the melting transition. Calculations of the heat capacity were performed on the nonequilibrium, instantaneous heating simulations, as well as on simulations of nanoparticles that were at equilibrium at the target temperature.

3 Results

3.1. The Bulk Modulus and Heat Capacity. The upper panel in Figure 2 shows the temperature dependence of the bulk

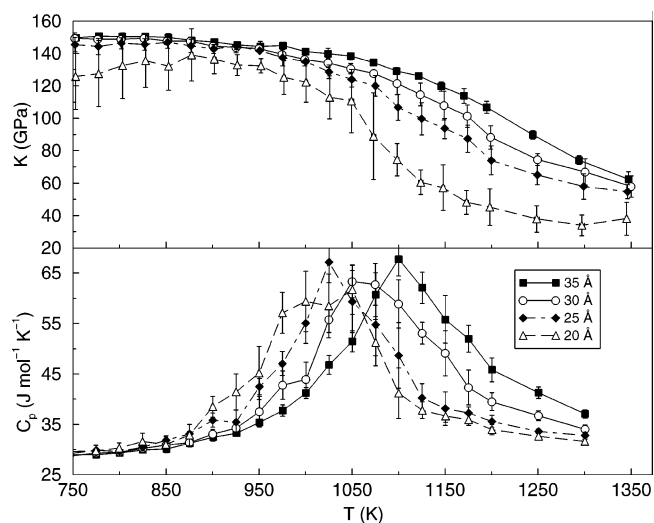


Figure 2. The temperature dependence of the bulk modulus (upper panel) and heat capacity (lower panel) for nanoparticles of four different radii. Note that the peak in the heat capacity coincides with the start of the softening of the bulk modulus.

modulus (K). In all samples, there is a dramatic (size-dependent) drop in K at temperatures well below the melting temperature of bulk polycrystalline gold. This drop in K coincides with the actual melting transition of the nanoparticles. Surface melting has been confirmed at even lower temperatures using the radial-dependent density, $\rho(r)/\rho$, which shows a merging of the crystalline peaks in the outer layer of the nanoparticle. However, the bulk modulus only has an appreciable drop when the particle melts fully.

Another feature of these transient (nonequilibrium) calculations is the width of the peak in the heat capacity. Calculation of C_p from longer equilibrium trajectories should indicate sharper features in C_p for the larger particles. Since we are initiating and observing the melting process itself in these calculation, the smaller particles melt more rapidly, and thus exhibit sharper features in C_p . Indeed, longer trajectories do show that T_m occurs at lower temperatures and with sharper transitions in larger particles than can be observed from transient response calculations. Figure 3 shows the results of 300 ps simulations which give much sharper and lower temperature melting transitions than those observed in the 40 ps simulations.

3.2. Breathing Mode Dynamics. Figure 4 shows representative samples of the volume vs time traces for the 20 and 35 Å particles at a number of different temperatures. We can clearly see that the period of the breathing mode is dependent on temperature, and that the coherent oscillations of the particles' volume are destroyed after only a few picoseconds in the smaller particles, while they live on for 10–20 ps in the larger particles. The decoherence is also strongly temperature dependent, with the high-temperature samples decohering much more rapidly than lower temperatures.

Although V vs t traces can say a great deal, it is more instructive to compute the autocorrelation function for volume fluctuations to give more accurate short-time information. Figure 5 shows representative autocorrelation functions for volume fluctuations. Although many traces exhibit a single frequency with decaying amplitude, a number of the samples show distinct beat patterns indicating the presence of multiple frequency components in the breathing motion of the nanoparticles. In particular, the 20 Å particle shows a distinct beat in the volume fluctuations in the 800 K trace.

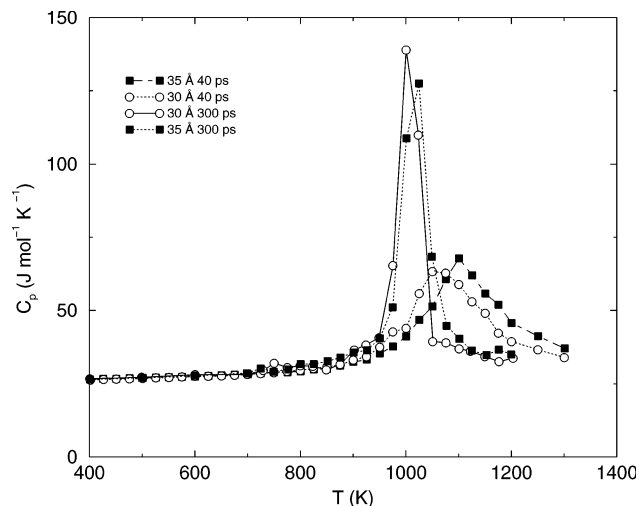


Figure 3. The dependence of the spike in the heat capacity on the length of the simulation. Longer heating-response calculations result in melting transitions that are sharper and lower in temperature than the short-time transient response simulations. Shorter runs do not allow the particles to melt completely.

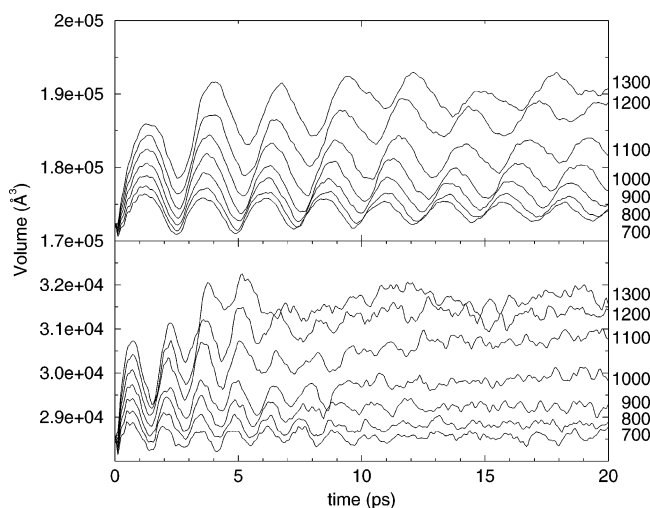


Figure 4. Sample volume traces for the 20 and 35 Å particles at a range of temperatures. Note the relatively rapid (<10 ps) decoherence due to melting in the 20 Å particle as well as the difference between the 1100 and 1200 K traces in the 35 Å particle.

When the power spectra of the volume autocorrelation functions are analyzed (eq 16), the samples which exhibit beat patterns do indeed show multiple peaks in the power spectrum. We plot the period corresponding to the two lowest frequency peaks in Figure 6. The smaller particles have the most evident splitting, particularly as the temperature rises above the melting points for these particles.

4. Discussion

Lamb's classical theory of elastic spheres³⁰ provides two possible explanations for the split peak in the vibrational spectrum. The periods of the longitudinal and transverse vibrations in an elastic sphere of radius R are given by

$$\tau_l = \frac{2\pi R}{\theta c_l} \quad (17)$$

and

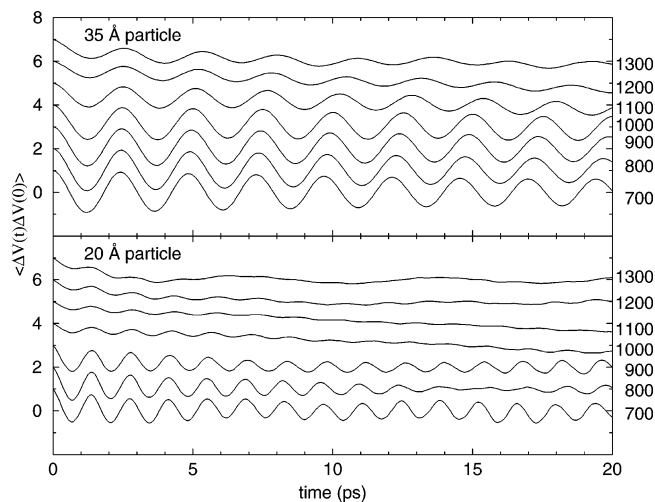


Figure 5. Volume fluctuation autocorrelation functions for the 20 and 35 Å particles at a range of temperatures. Successive temperatures have been translated upward by one unit. Note the beat pattern in the 20 Å particle at 800 K.

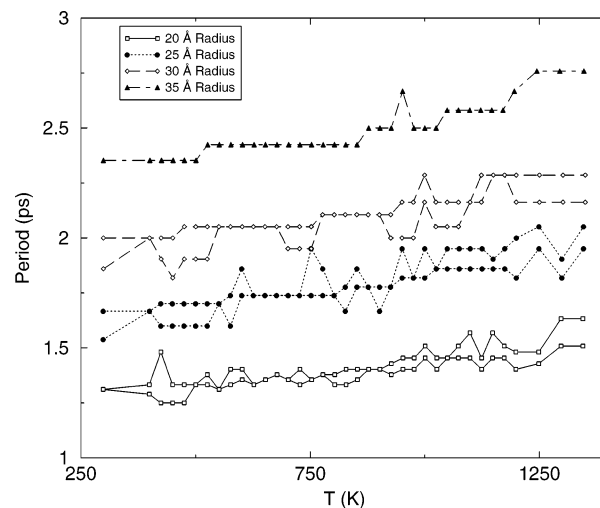


Figure 6. The temperature dependence of the period of the breathing mode for the four different nanoparticles studied in this work.

$$\tau_l = \frac{2\pi R}{\eta c_l} \quad (18)$$

where θ and n are obtained from the solutions to the transcendental equations

$$\tan \theta = \frac{3\theta}{3 - \theta^2} \quad (19)$$

$$\tan \eta = \frac{4\eta}{4 - \eta^2 \frac{c_l^2}{c_t^2}} \quad (20)$$

c_l and c_t are the longitudinal and transverse speeds of sound in the material. In an isotropic material, these speeds are simply related to the elastic constants and the density (ρ),

$$c_l = \sqrt{c_{11}/\rho} \quad (21)$$

$$c_t = \sqrt{c_{44}/\rho} \quad (22)$$

In crystalline materials, the speeds depend on the direction of propagation of the wave relative to the crystal plane.³¹ For

the remainder of our analysis, we assume the nanoparticles are isotropic (which should be valid only above the melting transition). A more detailed analysis of the lower temperature particles would take the crystal lattice into account.

If we use the experimental values for the elastic constants for 30 Å Au particles at 300 K, the low-frequency longitudinal (breathing) mode should have a period of 2.19 ps while the low-frequency transverse (toroidal) mode should have a period of 2.11 ps. Although the actual calculated frequencies in our simulations are off of these values, the difference in the periods (0.08 ps) is approximately half of the splitting observed for room-temperature simulations. This, therefore, may be an explanation for the low-temperature splitting in Figure 6.

We note that Cerullo et al. used a similar treatment to obtain the low-frequency longitudinal frequencies for crystalline semiconductor nanoparticles,³² and Simon and Geller have investigated the effects of ensembles of particle size on the Lamb mode using the classical Lamb theory results for isotropic elastic spheres.¹¹

4.1. Melted and Partially Melted Particles. Hartland et al. have extended the Lamb analysis to include surface stress (γ).¹² In this case, the transcendental equation that must be solved to obtain the low-frequency longitudinal mode is

$$\eta \cot \eta = 1 - \frac{\eta^2 c_l^2}{4c_l^2 - \frac{2\gamma}{(\rho R)}} \quad (23)$$

In ideal liquids, inclusion of the surface stress is vital since the transverse speed of sound (c_t) vanishes. Interested readers should consult Hartland et al.'s paper for more details on the extension to liquidlike particles, but the primary result is that the vibrational period of the breathing mode for liquid droplets may be written

$$\tau = \frac{2R}{c_l(l)} \quad (24)$$

where $c_l(l)$ is the longitudinal speed of sound in the liquid. Iida and Guthrie list the speed of sound in liquid Au metal as

$$c_l(l) = 2560 - 0.55(T - T_m) \text{ (ms}^{-1}\text{)} \quad (25)$$

where T_m is the melting temperature.³³ A molten 35 Å particle just above T_m would therefore have a vibrational period of 2.73 ps, and this would be markedly different from the vibrational period just below T_m if the melting transition were sharp.

We know from our calculations of C_p that the complete melting of the particles is *not* sharp, and should take longer than the 40 ps observation time. There are therefore two explanations which are commensurate with our observations.

1. The melting may occur at some time partway through observation of the response to instantaneous heating. The early part of the simulation would then show a higher frequency breathing mode than would be evident during the latter parts of the simulation.

2. The melting may take place by softening the outer layers of the particle first, followed by a melting of the core at higher

temperatures. The liquidlike outer layer would then contribute a lower frequency component than the interior of the particle.

The second of these explanations is consistent with the core-shell melting hypothesis advanced by Hartland et al. to explain their laser heating experiments.¹² At this stage, our simulations cannot distinguish between the two hypotheses. One possible avenue for future work would be the computation of a radial-dependent order parameter to help evaluate whether the solid-core/liquid-shell structure exists in our simulation.

Acknowledgment. The authors would like to thank Dr. Greg Hartland for a number of helpful discussions. P.F.C. was supported by an REU fellowship from the National Science Foundation. Computational time was provided on the Notre Dame Bunch-of-Boxes (B.o.B.) cluster under NSF grant DMR 00 79647. M.M.S., C.F.V., and J.D.G. acknowledge support under NSF grant CHE-0134881. We would also like to acknowledge helpful comments of one of the reviewers.

References and Notes

- Buffat, P.; Borel, J.-P. *Phys. Rev. A* **1976**, *13*, 2287–2298.
- Link, S.; Wang, Z. L.; El-Sayed, M. A. *J. Phys. Chem. B* **2000**, *104*, 7867–7870.
- Link, S.; El-Sayed, M. A. *J. Chem. Phys.* **2001**, *114*, 2362–2368.
- Shibata, T.; Bunker, B. A.; Zhang, Z.; Meisel, D.; Vardeman, C. F., II; Gezelter, J. D. *J. Am. Chem. Soc.* **2002**, *124*, 11989–11996.
- Del Fatti, N.; Voisin, C.; Chevy, F.; Vallee, F.; Flytzanis, C. *J. Chem. Phys.* **1999**, *110*, 11484–11487.
- Hodak, J. H.; Henglein, A.; Hartland, G. V. *J. Chem. Phys.* **1999**, *111*, 8613–8621.
- Hartland, G. V. *J. Chem. Phys.* **2002**, *116*, 8048–8055.
- Sader, J. E.; Hartland, G. V.; Mulvaney, P. *J. Phys. Chem. B* **2002**, *106*, 1399–1402.
- Hu, M.; Hartland, G. V. *J. Phys. Chem. B* **2002**, *106*, 7029–7033.
- Hu, M.; Hartland, G. V. *Proc. SPIE* **2002**, 4803.
- Simon, D. T.; Geller, M. R. *Phys. Rev. B* **2001**, *64*, 115412.
- Hartland, G. V.; Hu, M.; Sader, J. E. *J. Phys. Chem. B* **2003**, *107*, 7472–7478.
- Hodak, J. H.; Henglein, A.; Hartland, G. V. *J. Chem. Phys.* **2000**, *104*, 5053–5055.
- Voter, A.; Chen, S. *Mater. Res. Soc. Symp. Proc.* **1987**, *82*, 175.
- Daw, M. S.; Baskes, M. I. *Phys. Rev. B* **1984**, *29*, 6443–6453.
- Foiles, S. M.; Baskes, M. I.; Daw, M. S. *Phys. Rev. B* **1986**, *33*, 7983.
- Johnson, R. A. *Phys. Rev. B* **1989**, *39*, 12554.
- Lu, J.; Szpunar, J. A. *Philos. Mag. A* **1997**, *75*, 1057–1066.
- Finnis, M. W.; Sinclair, J. E. *Philos. Mag. A* **1984**, *50*, 45–55.
- Ercolessi, F.; Parrinello, M.; Tosatti, E. *Philos. Mag. A* **1988**, *58*, 213–226.
- Sutton, A. P.; Chen, J. *Philos. Mag. Lett.* **1990**, *61*, 139–146.
- Qi, Y.; Çagin, T.; Kimura, Y.; Goddard, W. A., III *Phys. Rev. B* **1999**, *59*, 3527–3533.
- Tartaglino, U.; Tosatti, E.; Passerone, D.; Ercolessi, F. *Phys. Rev. B* **2002**, *65*, 241406.
- Plimpton, S. J.; Hendrickson, B. A. *MRS Proc.* **1993**, *291*, 37.
- Hoover, W. G. *Phys. Rev. A* **1985**, *31*, 1695.
- Barber, C. B.; Dobkin, D. P.; Huhdanpaa, H. T. *ACM Trans. Math. Software* **1996**, *22*, 469–483.
- “Qhull”, 1993 software library is available from the National Science and Technology Research Center for Computation and Visualization of Geometric Structures (The Geometry Center), University of Minnesota: <http://www.geom.umn.edu/software/qhull/>.
- Berne, B. J.; Pecora, R. *Dynamic Light Scattering*; Dover Publications: Mineola, NY, 2000.
- Melchionna, S.; Ciccotti, G.; Holian, B. L. *Mol. Phys.* **1993**, *78*, 533–544.
- Lamb, H. *Proc. London Math. Soc.* **1882**, *13*, 189–212.
- Kittel, C. *Introduction to Solid State Physics*, 7th ed.; John Wiley and Sons: New York, 1996.
- Cerullo, G.; Silvestri, S. D.; Banin, U. *Phys. Rev. B* **1999**, *60*, 1928–1932.
- Iida, T.; Guthrie, R. I. L. *The Physical Properties of Liquid Metals*; Clarendon Press: Oxford, UK, 1988.